The Astrophysical Journal, 644:551–559, 2006 June 10

SPECTRUM OF A HABITABLE WORLD: EARTHSHINE IN THE NEAR-INFRARED

Margaret C. Turnbull,[1,2] Wesley A. Traub,[3,4] Kenneth W. Jucks,[4] Neville J. Woolf,[2,5] Michael R. Meyer,[2,5] Nadya Gorlova,[2,5] Michael F. Skrutskie,[6] and John C. Wilson[6]

Received 2005 November 11; accepted 2006 January 25

ABSTRACT

To characterize the spectrum of Earth viewed as an extrasolar planet, we observed the spatially integrated near-infrared (0.7–2.4 μm) reflection spectrum of Earth via the dark side of the Moon (earthshine). After contributions from the Sun, Moon, and local atmosphere were removed, the resulting spectrum was fitted with a simple model of the reflectivity of Earth. The best model fit is dominated by the reflection spectrum of the atmosphere above medium-altitude water clouds, with lesser contributions from high-altitude ice clouds and from the ground. The spectral features seen are H_2O (six strong band structures from 0.7 to 2.0 μm), CO_2 (six moderate-strength features from 1.4 to 2.1 μm), O_2 (two moderate-strength features at 0.76 and 1.26 μm), and several weak CH_4 features. Interpreted as a spectrum of an extrasolar planet, we would confidently conclude that this is a habitable planet, based on the presence of strong water bands. Furthermore, the simultaneous presence of oxygen and methane is a strong indicator of biological activity. We might also conclude that the planet is geologically active, based on the presence of CO_2, water, and a dynamic atmosphere (inferred from cirrus clouds, cumulus clouds, and clear-air fractions in our model fit). This suggests that it would be valuable for the *Terrestrial Planet Finder–Coronagraph* (*TPF-C*) mission to include near-infrared spectroscopy capability. On the basis of the present work, we suggest that future long-term monitoring of the earthshine would allow us to discern how the globally integrated spectrum changes with planet rotation, cloud cover, and seasons.

Subject headings: astrobiology — Earth — Moon — planetary systems

Online material: color figures

1. INTRODUCTION

1.1. *Observing Earth's True Colors*

What would the spectrum of a habitable extrasolar planet look like? Which atmospheric and surface signatures could be detectable? How would those signatures vary with planet rotation and seasonal changes? One of the key areas of research that will assist in the interpretation of extrasolar terrestrial planet spectra collected by NASA's *Terrestrial Planet Finder–Coronagraph* (*TPF-C*) mission is the study of the spatially integrated spectrum of our own planet, Earth. The goals of *TPF-C* (slated for launch around 2015) are to directly detect terrestrial planets around nearby stars, characterize the atmospheres and surfaces of these planets, and search for signs of life (Des Marais et al. 2002). In this paper we focus on the near-infrared spectral region that is potentially accessible to *TPF-C*. The present work is a continuation of our visible-wavelength earthshine observations (Woolf et al. 2002).

In the context of extrasolar planet research, the current best way to study the spectral characteristics of planet Earth is to observe earthshine, the faint light seen on the night side of the crescent Moon. Earthshine is light reflected from the sunlight-illuminated (day side) Earth onto the night side of the Moon and back again into our telescopes on the night-side Earth. Spectra taken via satellite observations are not adequate for viewing the globally integrated optical and near-infrared spectrum of Earth because most Earth-observing satellites see only small patches of ground at one time and usually observe in narrow wavelength bands that contain information about specific components of the reflection spectrum (e.g., the hydration level of vegetation or the presence of forest fires and resulting aerosols). Some Earth-observing satellites have covered the planet's whole surface in thousands of nadir-looking pointings (Burrows et al. 1999), but simply summing these spectra would not account for the changing path lengths through Earth's atmosphere and range of surface reflectance angles that are seen when observing the whole planet simultaneously.

1.2. *Previous Visible Light Observations*

In June of 2001, Woolf et al. (2002, hereafter Paper I) observed earthshine in the spectral range from 0.48 to 0.92 μm, with a resolution element of about 0.0008 μm. The view of Earth from the Moon during the observations was of a water-covered world: the Pacific Ocean dominated the visible illuminated area of the planet, and only about 17% of the projected area was covered by land (Australia, Alaska, and east Asia). The visible spectrum in Paper I has several indicators of what sort of planet this is. The increase in reflectivity toward shorter wavelengths, due to Rayleigh scattering, indicates the presence of an atmosphere. Water absorption bands indicate habitability. The oxygen absorption at 0.76 μm strongly suggests biological processes, especially combined with the tentative detection of the vegetation signal, represented by a sharp increase in reflectivity redward of 0.72 μm.

These features, as well as the overall brightness of the planet, are expected to vary with different views of the planet and changing cloud patterns. Montañés-Rodreguez et al. (2005) observed ~4% daily variations in Earth's broadband optical reflectivity due to clouds. Synthetic spectra from a model Earth generated

[1] Carnegie Institution of Washington, 5241 Broad Branch Road, Washington, DC 20008; turnbull@dtm.ciw.edu.
[2] NASA Astrobiology Institute Lead Team member.
[3] Jet Propulsion Laboratory, MS 301-451, 4800 Oak Grove Drive, Pasadena, CA 91109; wtraub@jpl.nasa.gov.
[4] Harvard-Smithsonian Center for Astrophysics, 60 Garden Street, Cambridge, MA 02138.
[5] Steward Observatory, University of Arizona, Tucson, AZ 85721.
[6] Department of Astronomy, University of Virginia, Charlottesville, VA 22903.

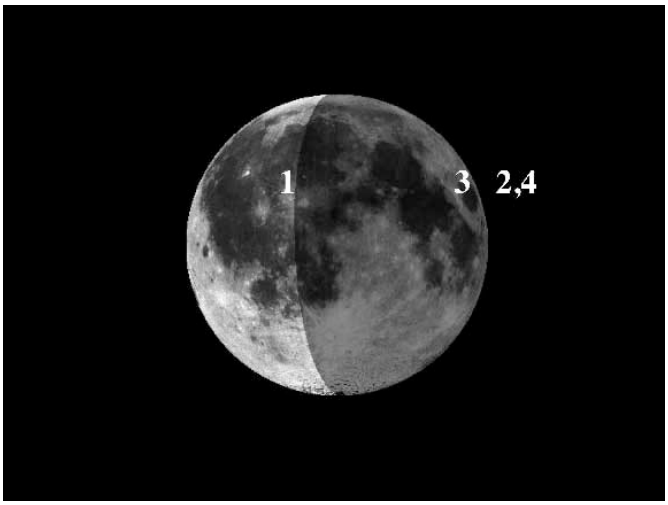

FIG. 1.—Appearance of the Moon on 2003 November 18, when the near-infrared data were taken. Approximate slit positions are shown on the bright Moon (1), nearby sky (2, 4), and dark Moon (3).

by Tinetti et al. show strong variations in the Earth's spectrum with changes in cloud cover (Tinetti et al. 2006a) and in the vegetation signal as the planet's continents rotate in and out of view (Tinetti et al. 2006b). This time variability may be the key to detecting weak surface signals on other planets (Seager et al. 2005).

In Paper I, a simple analysis of the visible-wavelength data was performed using a least-squares fit of several independent spectral components. The model included a wavelength-independent "high cloud" layer (assumed to be spectrally featureless at these wavelengths), a cloud-free model atmosphere of O_2, O_3, and H_2O, Rayleigh scattering, scattering from land plants, and much smaller amounts of reflection from ocean water, ocean pigments, and aerosol scattering. Given the distribution of landmass described above, it is not surprising that the vegetation signal appeared as a minor contributor (6% above the nearby continuum). Subsequent analysis of these data by Tinetti et al. (2006a) supported Paper I's conclusion that vegetation was detected and additionally identified a previously unsuspected signature of the oxygen dimer $(O_2)_2$ at 0.577 μm.

Section 2 provides the details of our near-infrared observing procedure and data reductions. In § 3 we present our near-infrared observations and model fit to the data, and in § 4 we summarize our conclusions and outline the work that is needed now to continue preparations for exoplanet-characterizing missions.

2. NEAR-INFRARED OBSERVATIONS

2.1. *Observing Procedure*

To expand our wavelength coverage of the Earth's spectrum, we obtained earthshine data in the near-infrared. Here we present earthshine observations in the spectral region 0.7–2.4 μm, at a resolution of about 300, with the Cornell-Massachusetts Slit Spectrograph (CorMASS), on the 1.8 m Vatican Advanced Technology Telescope at the Mount Graham International Observatory in southeast Arizona.

A computer-generated image of the Moon at the time of our observations is shown in Figure 1 (created with the Earth and Moon Viewer, by John Walker[7]). The dark side is weakly illuminated by sunlight reflected from the Earth, and this light contains the spectral imprint of Earth's atmospheric and surface features. We were not able to activate the lunar tracking rates on the telescope, so we positioned the slit and allowed it to trail across the Moon or sky during the observation, but the amount of total drift for each observation was quite small compared to the size of the Moon. We show approximate slit positions for our (1) bright-Moon (BM), (2, 4) near-sky (Sky_{near}), and (3) dark-Moon (DM) pointings. Our procedure was to observe

1. the bright limb of the Moon (~0.1 s exposures, 5–10 median-combined),
2. the sky near the dark side of the Moon (~200 s exposure),
3. the dark side of the Moon (~200 s exposure),
4. the sky near the dark side of the Moon (~200 s exposure, averaged with the previous sky observation to create Sky_{near}).

On the morning of 2003 November 18 (between 11:00 and 13:00 UT), eight such sets of data were successfully taken. We extracted an earthshine spectrum from each set (explained in the following sections), and the average of these was used in our model fit (§ 3).

The Earth, as seen from the perspective of the Moon (sub-observer coordinates N11°48′, W64°42′ at 11:30 UT) is shown in Figure 2, which depicts (*a*) a computer-generated image of surface features (also generated by the Earth and Moon Viewer) and (*b*) the cloud cover as seen by the *GOES-12* (*Geostationary Operational Environmental Satellite*) imager in channel 1 with a central wavelength of 0.65 μm (projection and data provided by the Space Science and Engineering Center,[8] University of Wisconsin–Madison; J. Robaidek 2005, private communication).

2.2. *Data Acquisition and Processing*

The CorMASS instrument is described in detail by Wilson et al. (2001), and the standard data reduction procedure can be found online.[9] CorMASS is a low-resolution ($R \sim 300$), cross-dispersed grating spectrograph; it normally operates from about 0.75 to 2.5 μm. In the present work we extracted an additional short-wavelength order, extending the coverage to 0.65 μm. But in our final spectrum we trimmed the range to 0.7–2.4 μm to remove noisy data on both ends and strong local thermal emission on the long-wavelength end. The sensor is a 256×256 pixel HgCdTe NICMOS3 detector; a flip mirror allows the lunar image and slit to be viewed together before each exposure.

In Figure 3 we show a typical two-dimensional dark-Moon spectrum, the difference of detector readouts before and after the integration (i.e., a double-correlated sampling sequence). The shortest wavelength (eighth) order is in the lower right, and the longest wavelength (first) order in the upper left. Within each order, wavelength increases from left to right.

The variable bias level, seen as a vertical background gradient in the upper and lower quadrants in Figure 3, is commonly referred to as the "NICMOS shading" or "reset decay pattern." This bias level depends on the time since last read, and thus it is different from image to image, but the shading in the lower quadrants is nearly identical to that in the upper quadrants. For each image, we used pixels from the upper quadrants that did not contain orders or ghosts of orders (from internal reflections) and interpolated these pixels to cover the entire detector, to create a full-frame bias image. The bias frame was then subtracted from the image.

[7] See http://www.fourmilab.ch/earthview/.

[8] See http://www.ssec.wisc.edu/datacenter/.

[9] See http://astrosun.tn.cornell.edu/research/projects/cormass/cormass.htm.

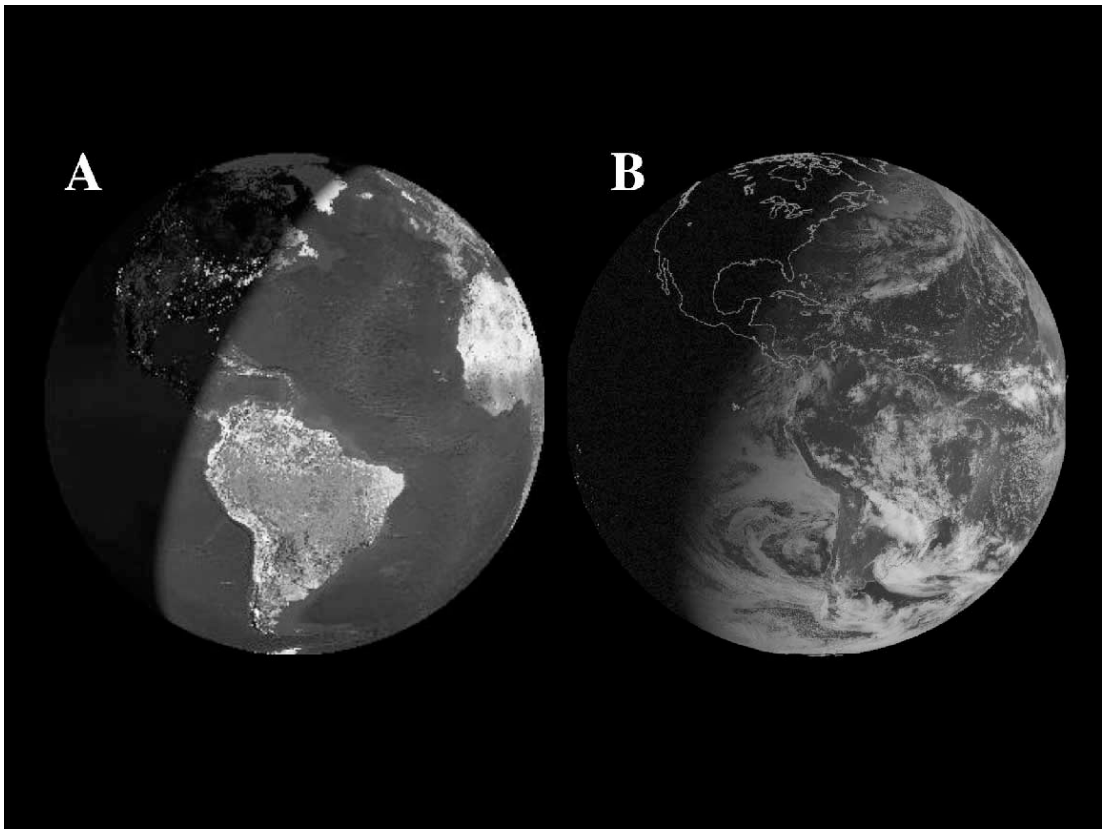

FIG. 2.—(*a*) Computer-generated view of Earth's surface as seen from the Moon at the time of our observations. (*b*) Cloud cover at the time of our observations, shown in approximately the same projection. [*See the electronic edition of the Journal for a color version of this figure*.]

FIG. 3.—Typical two-dimensional cross-dispersed raw spectrograph frame, showing the distribution of the spectral orders across the detector, as well as the underlying reset decay pattern, cosmic-ray hits, ghost images, and scattered-light background.

After bias subtraction, there was still a discontinuity between the upper and lower half of each image that was proportional to the amount of light contained in the brightest orders. We concluded from this that the lower half of the detector is more susceptible to scattered-light contamination than the upper half. To remove this discontinuity, a "step blank" was made using the 3 σ clipped average values of about 100 pixels between the brightest orders above and below the middle row.

After this initial processing, one-dimensional spectra were extracted using standard IRAF routines. We corrected bad pixels and cosmic-ray hits by interpolating along the slit. The locations of seven orders in the images, corresponding to wavelengths from 0.65 to 2.5 μm, were modeled with the IRAF task `apall`. We used a dark-Moon image as our template for locating the orders on all the data frames; the flat-field and bright-Moon images did not have enough counts in the shortest wavelength orders to be useful as a template. Once the order locations were defined, the remaining scattered-light background was satisfactorily removed using the IRAF routine `apscat` on all the images. (The `apscat` routine fits Chebyshev polynomials to interorder pixels and interpolates along lines and columns to estimate scattered-light levels within the orders, which are then subtracted.) One-dimensional spectra were created for each order by summing along the slit. Wavelength calibrations were carried out using emission lines from a planetary nebula observation, NGC 7027, from which a nearby sky spectrum was subtracted to remove airglow lines and thermal emission.

The seven extracted orders from the dark-Moon image in Figure 3 are shown in Figure 4; order 8 was dropped at this point because it had a poor signal-to-noise ratio. The overall intensity variation of each order is dominated by the grating diffraction

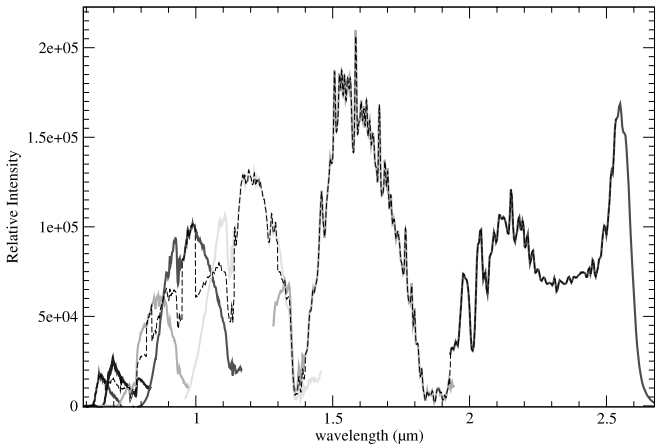

FIG. 4.—Data processing example. Individual one-dimensional orders (*solid lines*) extracted from the two-dimensional image in Fig. 3 were combined to give a single composite spectrum (*dashed line*), extending from 0.65 to 2.5 μm, and subsequently trimmed to the range 0.7–2.4 μm. The sharp discontinuities at order boundaries disappear completely upon dividing by the bright Moon, in a later step. [*See the electronic edition of the Journal for a color version of this figure*.]

pattern, with a peak in the center of an order and a minimum on either side; CorMASS orders are centered between major terrestrial absorption features, further reducing the apparent minima between orders. Solar and terrestrial lines are superposed. The spike near 2.5 μm is the Wien edge of the local thermal emission spectrum.

Orders were trimmed to remove any bad pixels at the ends. Our seven orders were then combined using the IRAF task `scomb` to create a single one-dimensional spectrum for each exposure (Fig. 4, *dashed line*). We determined wavelength boundaries for each order by eye, within which the signal-to-noise ratio appeared to be acceptably large, and we constructed the composite spectrum using a straight average of contributing orders (where orders overlapped in wavelength). All spectra were processed with identical boundary values for each order. This left us with large discontinuities at wavelengths corresponding to the edges of the trimmed orders, but these discontinuities exactly cancel when the data are ratioed to the bright-Moon spectrum. (This could also be accomplished by dividing all the data by a flat-field frame.)

2.3. *Extracting the Earthshine Spectrum*

In brief, we extract the earthshine spectrum by (1) subtracting the scattered moonlight, airglow, and thermal emission of our local atmosphere from the dark-Moon spectrum and (2) dividing the result by the bright Moon. Dividing the sky-subtracted dark Moon by the bright Moon serves four purposes: (1) it flat-fields the data (removes nonuniformities in detector response), (2) it divides out the solar spectrum, (3) it divides out the lunar spectrum except for the lunar phase function effect (explained in § 2.5), and (4) it divides out atmospheric absorption from the final pass through the Earth's atmosphere from the dark Moon to our telescope. No sky is subtracted from the bright limb because the sky contributions are negligible in such short integrations ($\sim$0.1 s).

Mathematically, the earthshine spectrum [ES(λ)] is extracted as follows:

$$\mathrm{ES} = \left(\frac{\mathrm{DM}^* - \mathrm{Sky}_{\mathrm{DM}}}{\mathrm{BM}^*}\right)\left(\frac{R_{\mathrm{BM}}}{R_{\mathrm{DM}}}\right), \quad (1)$$

where

$$\mathrm{DM}^* = \mathrm{Sun} \times R_{\mathrm{Earth}} R_{\mathrm{DM}} T_{\mathrm{atm}} + \mathrm{Sky}_{\mathrm{DM}}, \quad (2)$$

$$\mathrm{BM}^* = \mathrm{Sun} \times R_{\mathrm{BM}} T_{\mathrm{atm}}, \quad (3)$$

$$\mathrm{Sky}^*_{\mathrm{far}} = \mathrm{airglow} + \mathrm{thermal\ background\ emission}, \quad (4)$$

$$\mathrm{Sky}_{\mathrm{DM}} = \mathrm{Sky}^*_{\mathrm{far}} + \mathrm{Sky}_{\mathrm{scatt,\,DM}}, \quad (5)$$

$$\mathrm{Sky}_{\mathrm{scatt,\,DM}} = f\,\mathrm{Sky}_{\mathrm{scatt}}, \quad (6)$$

$$\mathrm{Sky}_{\mathrm{scatt}} = \mathrm{Sky}^*_{\mathrm{near}} - \mathrm{Sky}^*_{\mathrm{far}}. \quad (7)$$

All quantities (except f, over these small angles) are a function of wavelength, and observed quantities are indicated with an asterisk. The quantity DM* is the measured dark-Moon spectrum (position 3 in Fig. 1), and it contains the spectrum of the Sun, the single-pass transmission spectrum of the Earth's atmosphere from the Moon to the telescope (T_{atm}), the reflection spectrum of the Earth (R_{Earth}, globally integrated, including reflection from all cloud and surface types and including atmospheric absorption), and the reflection spectrum of the dark moon at 0° phase angle (R_{DM}), as well as an additive term contributed by local airglow, thermal emission, and scattered moonlight. The quantity BM* is the measured bright-Moon spectrum, and it contains the spectrum of the Sun, the reflection spectrum of the bright Moon (R_{BM}) at the Sun-Moon-Earth phase angle ($\sim$120°), and T_{atm}. The quantities R_{DM} and R_{BM} differ only in that the reflectance spectrum of the Moon is redder at larger phase angles (see § 2.5). The observed sky spectra are $\mathrm{Sky}^*_{\mathrm{far}}$ (the sky spectrum as it would be without the contribution of scattered moonlight, measured at about the same elevation as the Moon observations, but several hours before moonrise) and $\mathrm{Sky}^*_{\mathrm{near}}$ (the sky spectrum measured near the limb of the dark Moon, which contains slightly less scattered moonlight than the dark-Moon spectrum does). The spectrum of scattered light present in the $\mathrm{Sky}_{\mathrm{near}}$ observation, $\mathrm{Sky}_{\mathrm{scatt}}$, is calculated by subtracting $\mathrm{Sky}_{\mathrm{far}}$ from $\mathrm{Sky}_{\mathrm{near}}$. The amount of scattered-light contribution at the position of the DM spectrum is slightly greater than this and is represented by a near-unity multiplier f times $\mathrm{Sky}_{\mathrm{scatt}}$. The functional form of $\mathrm{Sky}_{\mathrm{scatt}}$ is inferred by least-squares fitting, described in § 2.4, and the factor f is a free parameter in our model fit (§ 3). $\mathrm{Sky}_{\mathrm{DM}}$, then, is equal to the $\mathrm{Sky}_{\mathrm{far}}$ observation plus this appropriately scaled scattered-light contribution.

Substituting into equation (1), the ES spectrum gives us a measurement of the spatially integrated spectrum of the sunlit and geometrically visible Earth, as it would be seen from another star system:

$$\mathrm{ES} \approx R_{\mathrm{Earth}}. \quad (8)$$

In the following figures, all spectra are shown after division by the BM spectrum and after scaling by the relative lengths of exposures where appropriate.

2.4. *Subtracting the Local Sky Contribution,* $\mathrm{Sky}_{\mathrm{DM}}$

The sky spectrum at the location of the slit on the dark Moon, which we refer to as $\mathrm{Sky}_{\mathrm{DM}}$, contains three additive components of the local atmosphere that must be removed: airglow emission lines, thermal background emission, and scattered light from the bright Moon. Scattered moonlight (an additive component) accounts for about half the signal at the dark-Moon position, and its subtraction is complicated by the fact that the amount of scattered moonlight varies with angle from the bright crescent

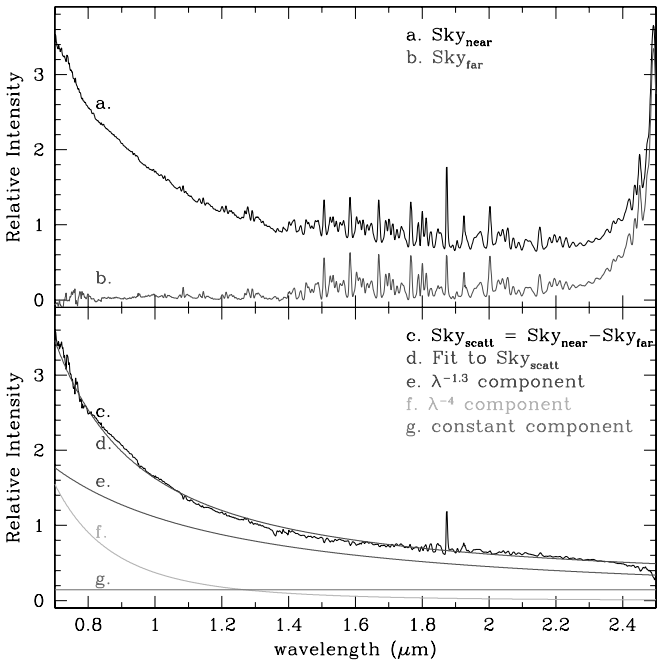

FIG. 5.—*Top:* Observed sky spectra near the dark Moon (Sky_{near}; *curve a*) and far from the Moon (Sky_{far}; *curve b*). The Sky_{far} spectrum is dominated by OH emission bands centered at the 1.5–2.1 μm region and thermal background emission longward of about 2.2 μm. *Bottom:* The scattered moonlight spectrum, Sky_{scatt} (*curve c*), along with a least-squares fit (*curve d*) including the sum of a Rayleigh-scattering term (λ^{-4}; *curve f*), an aerosol term ($\lambda^{-1.3}$; *curve e*), and a constant term (*curve g*). [*See the electronic edition of the Journal for a color version of this figure*.].

Moon, whereas airglow and thermal emission (also additive) do not; we account for each of these components as follows.

The airglow plus thermal background spectrum was measured by observing apparently blank sky, at approximately the same elevation as the Moon, but before moonrise to avoid any scattered moonlight component. This spectrum is shown in Figure 5 (*curve b*). The spectrum is dominated by the well-known emission bands of OH, originating in the upper stratosphere and extending from at least 1.07 to 2.27 μm. A high-resolution OH spectrum of this wavelength region was obtained by Oliva & Origlia (1992), from which it is clear that the smallest features in our spectrum, for example near, 1.08, 1.14, and 1.21 μm, are all real and are due to OH.

The sky spectrum near the dark Moon (Sky_{near}) is also shown in Figure 5 (*curve a*). The OH emission and the thermal background are present in both the Sky_{far} and Sky_{near} spectra, and these features match quite closely, even though they were taken in quite different regions of the sky. The thermal background emission is seen in both spectra as a steep increase in intensity starting around 2.2 μm and going off-scale past 2.4 μm. Most of this flux probably originates in the telescope and spectrometer.

The difference spectrum, $Sky_{near} - Sky_{far}$, is shown in the lower panel of Figure 5. We show that this spectrum can be attributed to a total of three types of atmospheric scattering of moonlight, so for convenience we call it the scattered-light spectrum, $Sky_{scatt} = Sky_{near} - Sky_{far}$. The Sky_{scatt} spectrum decreases monotonically with increasing wavelength, except for slight departures at the extreme short-wavelength end (where the signal-to-noise ratio is low), long-wavelength end (where thermal blackbody emission dominates), and a narrow spike at 1.87 μm, due to imperfect subtraction of the strong and highly time-variable OH feature.

The Sky_{scatt} spectrum suggests that two physical mechanisms might be present here: Rayleigh scattering of moonlight by molecules in the air path above the telescope and aerosol scattering of moonlight by small particles suspended in the air above the telescope. To test this hypothesis, we did a least-squares fit of the difference spectrum to a function of the form $\lambda^{-4} + a\lambda^{-1.3} + b$. Here λ is in microns, and the exponent of the aerosol term is the same as we used in Paper I and is suggested in Allen (1991). The constant term is an empirical adjustment with no obvious physical basis (although it could conceivably arise from scattered light within the spectrograph) but without which the residuals from a least-squares fit are approximately doubled. We find the aerosol coefficient $a \sim 2.99$, and the constant $b \sim 0.38$. These spectral contributions are shown in Figure 5 (*bottom*), along with their sum as a fit to the data. For wavelengths $\lambda > 0.7$ μm the aerosol term dominates Rayleigh scattering, and for $\lambda > 1.3$ μm the constant term also dominates Rayleigh scattering.

To remove the sky spectrum (Sky_{DM}) from the observed dark-Moon spectrum (DM) we subtract the airglow and thermal background spectrum (Sky_{far}), and we separately subtract the scattered-light spectrum Sky_{scatt}, scaled by a factor f. The expectation is that the scattered flux increases closer to the source of the light, the bright Moon, so $f > 1$ for the position of the dark Moon relative to the near-sky observation. In § 3, we find the factor f by simultaneously fitting the dark-Moon spectrum to a theoretical model of the earthshine spectrum plus a scaled copy of the scattered-light spectrum. We find that the best fit occurs for $Sky_{scatt,DM} = (1.10 \pm 0.02)Sky_{scatt}$, showing that the scattering is about 10% stronger at the slit position on the dark limb than it is at the slit position on the nearby sky.

2.5. *Lunar Reflectance Correction*

The factor R_{BM}/R_{DM} in equation (1) accounts for the fact that the reflectance spectrum of the Moon varies with the angle of incidence and reflection. Ideally, we would have full bidirectional reflectance data for the lunar surface as a function of the surface type (mare, highlands, etc.) and wavelength. In reality, we have data on the broadband reflectance color as a function of lunar phase angle. Lane & Irvine (1973) measured the integrated lunar geometric albedo as a function of phase angle (from 6° to 120°) and wavelength (nine narrow bands from 0.35 to 1.0 μm, plus *UBV*). T. Stone & H. T. Kieffer (2006, in preparation) measured the lunar disk reflectance as a function of phase angle (2°, 32°, 62°, and 92°) and wavelength (0.35–2.4 μm). Combining both sets of data and extrapolating to our phase angles (roughly 120° for BM and 0° for DM), we find the following reflectance correction factor:

$$\frac{R_{BM}}{R_{DM}} = \text{constant} \times (1 + 0.42\lambda), \tag{9}$$

where λ is in microns and the range of validity is roughly 0.7–2.4 μm. (For $\lambda < 0.7$ μm the ratio is smaller than this relation would indicate.) Over the range of our spectra, this correction factor varies by a factor of about 1.55, so our corrected ES spectrum is "redder" than the uncorrected spectra.

3. SPECTRUM MODEL AND ANALYSIS

Figure 6 shows the finally extracted earthshine spectrum (*black line*), averaged from a total of eight spectra taken over the course of 2 hr on the morning of 2003 November 18. Our spectroscopic model (*red line*) is a modified version of the model that we developed in Paper I for the analysis of visible spectra. The radiative transfer code is described in Traub & Jucks (2002) and

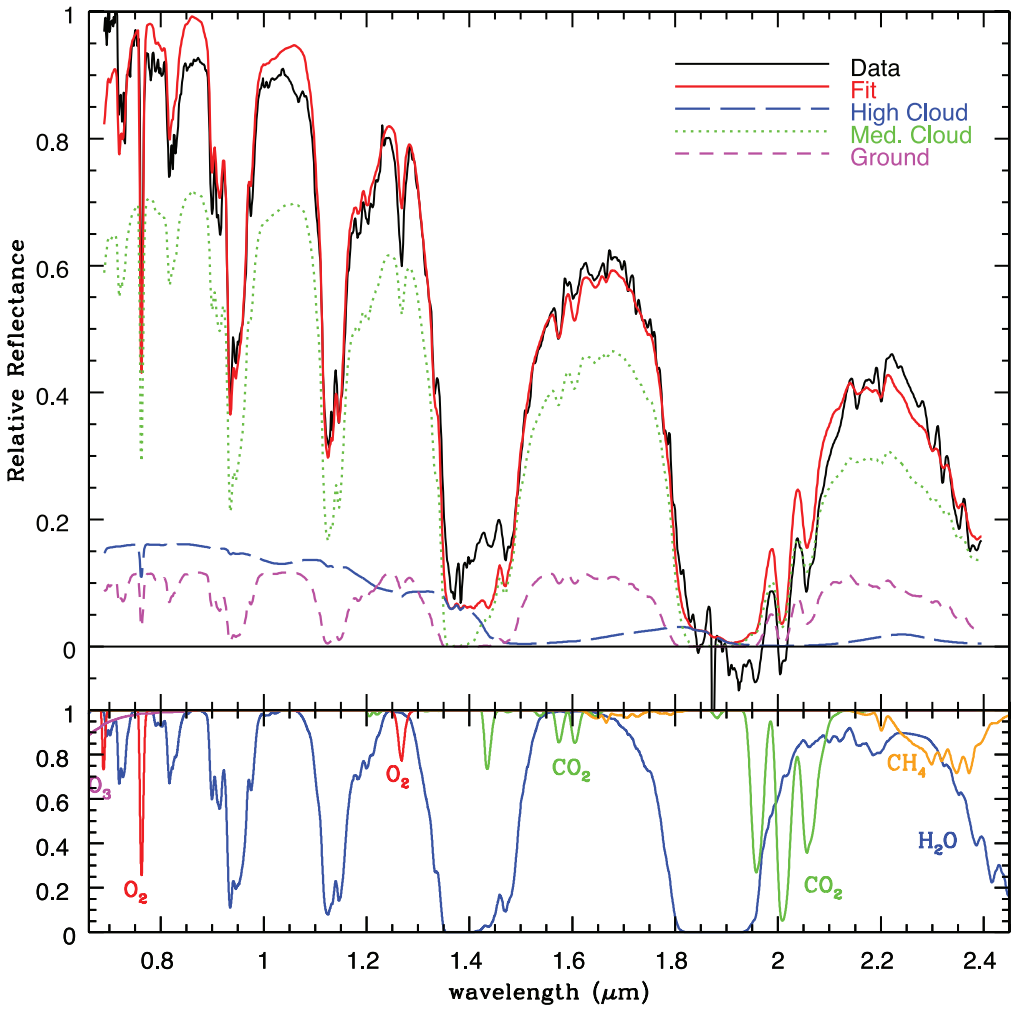

FIG. 6.—*Top:* Near-infrared reflectance spectrum of the integrated Earth. The black solid line is the observed spectrum, scaled to a convenient value. The red line is the fitted spectrum, a sum of the following three streams: (1) "high cloud" (*blue long-dashed line*), based on cirrus ice particles at a fixed altitude of 10 km, and the overlying air mass; (2) "medium cloud" (*green dotted line*), based on a cumulus water cloud at a fitted altitude of 4 km, and the overlying air mass; and (3) a "ground" reflectance (*magenta short-dashed line*), based on a gray surface at a fixed altitude of 0 km, and the overlying air mass. *Bottom:* Major molecular components for comparison, showing clear-atmosphere spectra of water (*blue line*), carbon dioxide (*green line*), methane (*orange line*), oxygen (*red line*), ozone (*magenta line*), and nitrous oxide (negligible, not shown).

Traub & Stier (1976). We use standard mixing ratios of H_2O, O_2, O_3, etc., and a standard, midlatitude, model atmosphere (pressure and temperature as a function of altitude), divided into thin layers from 0 to 100 km altitude. The spectrum is calculated at very high spectral resolution, with several points per line width, where the line shapes and widths are computed using Doppler and pressure broadening on a line-by-line basis, for each layer in the model atmosphere. The overall high-resolution transmission spectrum is then calculated, and smoothed and sampled to match the experimental wavelength grid and resolution. For references and further explanation, the reader is referred to our calculation of a complete set of molecular constituent spectra, for a wide range of mixing ratios, for the present Earth pressure-temperature profile, for the visible and thermal infrared, in Des Marais et al. (2002).

3.1. *Model Components*

Our goal in the present analysis is to model the data with a minimum number of parameters. We use a simple geometrical model in which the illuminated part of the spherical Earth is modeled with a single angle of incidence and reflection, selected to give the best analytical approximation to the integrated-Earth air-mass factor for a nominal illumination situation (quadrature); the zenith angle of this ray is 60°. We assume that the complex cloud distribution, horizontally and vertically, can be approximated by three parallel streams, all at the same angle, all traversing the same molecular atmosphere, but with each stream reflecting from a different altitude surface.

The first stream reflects from the planet's surface at 0 km altitude, the second stream reflects from a cloud layer with a top at an adjustable height (here 4 km), and the third stream reflects from a cloud at a high altitude, fixed at 10 km. The relative proportions of each stream are adjusted in a least-squares fit to the full reflectance spectrum.

The 0 km stream, called "ground," is assumed to reflect from a gray surface. In preliminary fits that included vegetated spectra, the fitted proportion was always very small, so in our subsequent fits, we eliminated the vegetated spectral component, to minimize the number of adjustable parameters. The mixing ratios of the molecular atmospheric constituents were fixed. Only the fraction of the total flux in this stream was varied. As shown in Figure 6, the contribution of this stream is small but nonnegligible, being

about 12% of the total reflectivity at a typical point in the continuum around 1.05 μm.

The 4 km stream, called "medium cloud," is assumed to reflect from a cumulus cloud of water droplets. The reflectance spectrum of this cloud is taken from the calculations for 8 μm water droplets shown in Figure 3 of King et al. (1997; see also King et al. 1990 for details); it is dominated by absorption features that closely resemble strong water bands. The molecular atmosphere is as above. In preliminary fits, with this cloud top at 6 km (as in Paper I), we were unable to make a satisfactory fit to the water bands at 0.94 and 1.13 μm, the fitted lines being too weak. In a few trials, we found that the fit improved dramatically if we moved the cloud top to 4 km, so we fixed the cloud at that level. The effect on the strong bands at 1.41 and 1.88 μm was small. As shown in Figure 6, this stream contributes the bulk of the reflectivity signal, about 74% of the total at 1.05 μm.

The 12 km stream, called "high cloud," is assumed to reflect from a cirrus cloud of ice particles, the reflectance of which is from the experimentally measured data in Barkey et al. (2000). The spectrum of this cloud decreases at long wavelengths and has derivative-like features at the locations of the two strongest water absorption bands, as can be gleaned from Figure 6; the spectrum is distinctly different from that of a liquid-phase cloud. This stream contributes a modest amount, about 14%, at 1.05 μm.

3.2. *Model Uncertainties*

The reflectance spectra of all three surfaces should be considered as only first approximations to reality, for several reasons. For example, for the cumulus and cirrus spectra, the literature contains a variety of cloud spectra that presumably represent a variety of real clouds but that also may represent a variety of experimental conditions. Parameters that are desirable to know but that are often not specified include the following: the angle of incidence, the angle of reflection, the cloud thickness, the effects of multiple scattering, the degree of homogeneity of the cloud, the frequency of occurrence of a given type of cloud, and the altitude at which a given cloud might form. An additional uncertainty in published cloud spectra is the degree to which the transmission spectrum of the free atmosphere has been removed from the cloud data.

A more detailed model would be worth constructing as part of a model-validation exercise, but it would require a large modeling effort and should include the actual cloud-height and cloud-type distribution at the time of observation. The present work demonstrates that a simple model can be constructed that adequately represents the observed spectrum, but the question remains as to whether that model in fact reflects reality. It is for this reason, validating that we can in fact reconstruct the Earth's spectrum given accurate information about clouds and surface types, that it would be worthwhile to construct a more detailed model.

The rms uncertainty of the spectrum in Figure 6 can be estimated from the rms scatter in the eight individual spectra that were averaged to produce the spectrum. This rms scatter is about 3% of the median peak intensity of all eight spectra, and it is surprisingly uniform across all wavelengths, showing no noticeable variation from blue to red or from continuum to deep absorption features. A histogram of the variations shows a profile intermediate between a Gaussian and a triangle function. Two exceptions are at the deepest water bands at 1.36–1.37 and 1.85–1.92 μm, where the rms scatter jumps sharply up to $\sim$10%. The otherwise uniform scatter suggests that the rms scatter is caused by random-noise variations in the data (e.g., slight variations in scattering caused by subvisual hazes). The resulting error in the mean is then about 1.1% at a typical point in the spectrum. Using this estimate, the reduced χ^2 value for the data and model fit shown in Figure 6 is 0.9. This is obtained by fitting 1487 data points in the 0.7–2.4 μm region and allowing for four effectively adjustable parameters (ground, medium cloud, high cloud, and scattered light). This small value of χ^2, near unity, suggests that our estimate of the uncertainty in the spectrum is appropriate.

3.3. *Insights from the Near-Infrared Earthshine Spectrum*

The dominant spectral signatures in the 0.7–2.4 μm region of the Earth's reflection spectrum are H_2O, O_2, CO_2, and cirrus cloud. The weaker features from CH_4 and even CO_2 do not dominate the present Earth spectrum but could be much stronger on another planet or in an early-Earth spectrum.

For H_2O, we see that the six vibrational bands in this range (0.72, 0.82, 0.94, 1.13, 1.41, and 1.88 μm) get dramatically stronger toward longer wavelengths. So for an extrasolar planet with much less water than the Earth, or for additional validation of the water bands in the visible, the near-infrared region is an excellent source of information.

For O_2, the strong bands at 0.76 and 1.27 μm both show up quite clearly at the present spectral resolution; at lower resolution these bands would still be potentially measurable.

The CO_2 features in this spectrum are seen with moderate strength at 1.44 μm (one feature) and 1.59 μm (two features) and quite strongly at 2.03 μm (three features). The weak bands at 1.05 and 1.21 μm are essentially invisible at the present CO_2 abundance on Earth, but on an early-type Earth they would be candidates for detection.

The CH_4 features in this spectrum are at 1.69 and 2.32 μm; however, neither of these appear with any clarity in the measured spectrum, owing to weakness and breadth, respectively. On an early Earth these bands would be much stronger, and in addition the CH_4 features at 0.73, 0.79, 0.89, and 1.00 μm would become detectable, with the longer wavelength bands being the strongest.

The other two species considered in this study are O_3 and N_2O. Ozone absorption becomes significant at our shortest wavelengths, growing to $\sim$10% at 0.7 μm. At our resolution, the strongest feature of N_2O is smaller than 0.5%, at 2.4 μm.

The cirrus cloud spectrum used for our "high cloud" component is an element in the present data that was not anticipated in the Des Marais et al. (2002) study, since the latter focused on molecular species. It was also not anticipated from the visible earthshine spectrum because cirrus and cumulus clouds both have approximately constant reflectance in the visible, as best we can determine from the literature (e.g., King et al. 1997, 1990; Knapp et al. 2002). In the near-infrared, cirrus and cumulus clouds are spectrally distinct, and the cirrus spectrum is an important near-infrared feature to consider for extrasolar planet work. Indeed, coverage at near-infrared wavelengths is critical to Earth-observing satellites in distinguishing between cirrus clouds, cumulus clouds, and snow cover (Krijger et al. 2005). However, given a single spatially integrated spectrum and no other information, it may be impossible to distinguish cirrus clouds from icy surfaces (see Carlson et al. 1996; Cruikshank et al. 2005 for spectra of the icy Jovian and Saturnian satellites). Our model did not include any snow- or frost-covered ground; this did not seem necessary given the view of Earth in Figure 2, and we have attempted to keep our model as simple as possible.

Cumulus clouds show a water-like spectrum, so they are not easily distinguishable from water vapor itself; however, further work may show cumulus to be detectable as well, assuming that

we can separate these spectra. The presence of cumulus clouds suggests an active troposphere, with convective upwelling and down-welling, and the existence of weather patterns that might be detected with long-term observations.

Finally, we note that the vegetation signal did not appear to be present at a detectable level in these data. This is perhaps surprising, given the view of Earth shown in Figure 2. As mentioned in § 1, the vegetation signal is represented by a sharp increase in reflectivity redward of 0.72 μm, and the optical data presented in Paper I appear to show this feature. However, plant reflectance falls off again in the near-infrared due to liquid water vibrational absorption features (see Clark 1999). In fact, the near-infrared spectrum of plants is very similar to that of clouds, which may explain why we were not able to clearly identify it in our data. At $\sim$0.7 μm, where we would expect to see the vegetation "jump," the signal-to-noise ratio of our data was very low, and we cannot claim any clear contribution from plants to our near-infrared earthshine spectrum.

4. CONCLUSIONS AND FUTURE WORK

In Figure 7, we present the combined data from Paper I and the new observations presented here. The optical data have been smoothed to match the resolution of the near-infrared data, and the two data sets were merged at 0.8 μm. The entire data set was then normalized to 1.0 at 0.5 μm. At these wavelengths, our world is spectrally distinct from Venus and Mars (Traub 2003; Mustard & Bell 1994; Klassen et al. 1999), the gas giant planets (Fink & Larson 1979), and their satellites (Carlson et al. 1996; Cruikshank et al. 2005). What can we say about the Earth, based on these data? First, from the strong water bands, we would confidently conclude that Earth is a habitable planet. Furthermore, the simultaneous detection of methane and abundant oxygen is strongly suggestive of either biological activity or some unusual atmospheric or geological process that can sustain large amounts of atmospheric oxygen in the presence of reduced gases (e.g., a "runaway greenhouse" situation as described by Kasting et al. [1993] could generate a large oxygen signal, but only for a short period of time). From the clear-air and cloud fractions required in our model to fit the data, we would also conclude that the planet has a dynamic atmosphere. Thus, the spectral albedo could be expected to show slight changes with time, and with long-term monitoring we may be able to deduce the planet's timescale for weather patterns. We could also expect to see periodic changes due to planet rotation if the surface has strong nonuniformities, and we could hope to constrain continental and ocean cover, perhaps even mineral types or hints of pigments in widespread photosynthetic organisms.

Given these conclusions, it is advisable to consider endowing the *TPF-C* mission with the capability of working in the near-infrared. This would place an additional burden on the mission, in terms of a detector and spectrometer, and it would not be possible to reach as close to the star as would be desired in all cases, owing to the diffraction limitation of a few times λ/D of most coronagraphs (where D is the diameter of the telescope). Furthermore, the decreasing planetary reflectance at these wavelengths may lengthen exposure times for detection. A thorough assessment of the observations that would be possible at near-infrared wavelengths, with various choices of coronagraph and for stars in the solar neighborhood, would tell whether it is worthwhile to have a near-infrared capability on *TPF-C*.

Two lines of observational work that need a better understanding for interpreting earthshine data are (1) a more rigorous study of the scattered-light sky spectrum and the way in which it changes with position relative to the bright Moon and (2) a better understanding of the spectra of different types of clouds.

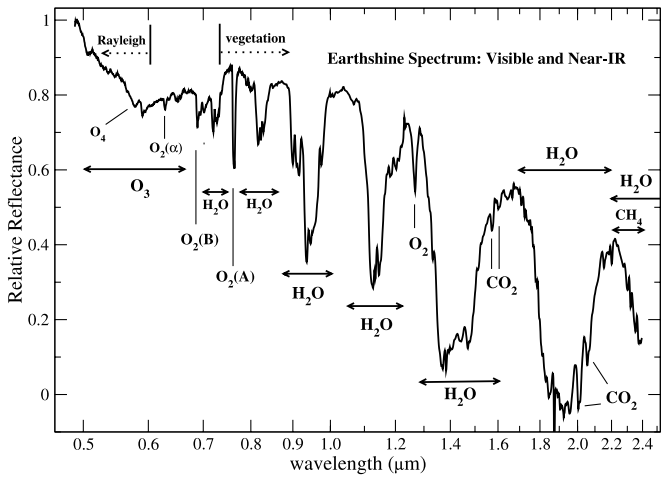

FIG. 7.—Earth's observed reflectance spectrum, at visible and near-infrared wavelengths, created from a composite of the data in this paper (0.8–2.4 μm) and the data presented in Paper I (0.5–0.8 μm). The strongest molecular signatures are indicated, as are the wavelengths where Rayleigh scattering and vegetation reflection are most significant.

In terms of validating models that reconstruct the Earth based on its spectrum, we need to know, what is the full range of parameters, in terms of cloud types, cloud heights, atmospheric water content, abundances of other gaseous components, and surface compositions, that will generate a satisfactory fit to the data, within the observational uncertainties? It is important to clearly map out the degeneracies between the different components of our models, so that we can understand the likelihood that a given model reflects reality when we begin to characterize extrasolar planets.

Many other insights could result from the study of how the Earth's spectrum changes over time. For example, periodic changes due to planet rotation could be used to create a map of fractional land and ocean area as a function of longitude (see Ford et al. 2001). We must also ask, how much does cloud cover wash out spectral signatures of the surface? Seasonal changes, and even changes associated with atmospheric chemistry in response to the Solar transient events and cycles, are interesting topics that may be relevant to the interpretation of terrestrial exoplanet spectra and would also contribute to our understanding of the Earth-Sun system. A long-term earthshine monitoring campaign, covering all longitudes and seasons, would be a crucial part of preparing for the launch of *TPF-C*. However, if such a campaign requires contributions from multiple observatories, great care must be taken to account for different instrumental and local atmospheric effects before we can confidently interpret the spectrum of our planet's many faces.

We thank Lisa Kaltenegger and Sara Seager for comments on the manuscript. This work was supported in part by NASA grant NAG5-13045 (W. T.). M. C. T. was supported by a postdoctoral fellowship from the NASA Astrobiology Institute and the National Research Council. M. C. T. also thanks J. Lunine for support of this work, as well as J. Kasting, P. Montañés-Rodriguez, and G. Tinetti for sharing their insights. We are grateful to C. Corbally, S. J., of the Vatican Observatory, and to M. Nelson for their help with 1.8 m VATT operations. We would also like to thank the anonymous referee for several helpful suggestions.

REFERENCES

Allen, C. W. 1991, Astrophysical Quantities (3rd ed.; London: Athlone), 126
Barkey, B., Liou, K. N., Takano, Y., & Gellerman, W. 2000, Appl. Optics, 39, 3561
Burrows, J. P., et al. 1999, J. Atmos. Sci., 56, 151
Carlson, R., et al. 1996, Science, 274, 385
Clark, R. N. 1999, in Manual of Remote Sensing, Vol. 3: Remote Sensing for the Earth Sciences, ed. A. N. Rencz (New York: Wiley), 3 (http://speclab.cr.usgs.gov/PAPERS.refl-mrs/refl4.html)
Cruikshank, D. P., et al. 2005, Icarus, 175, 268
Des Marais, D. J., et al. 2002, Astrobiology, 2, 153
Fink, U., & Larson, H. 1979, ApJ, 233, 1021
Ford, E. B., Seager, S., & Turner, E. L. 2001, Nature, 412, 885
Lane, A. P., & Irvine, W. M. 1973, AJ, 78, 267
Kasting, J., Whitmire, D., & Reynolds, R. 1993, Icarus, 101, 108
King, M. D., Radke, L. F., & Hobbs, P. V. 1990, J. Atmos. Sci., 47, 894
King, M. D., Tsay, S.-C., Platnick, S. E., Wang, M., & Liou, K.-N. 1997, Cloud Retrieval Algorithms for MODIS: Optical Thickness, Effective Particle Radius, and Thermodynamic Phase (MODIS Algorithm Theor. Basis Doc. No. ATBD-MOD-05; Greenbelt: NASA GSFC), http://modis-atmos.gsfc.nasa.gov/_docs/atbd_mod05.pdf
Klassen, D. R., Bell, J. F., III, Howell, R. R., Johnson, P. E., Golisch, W., Kaminski, C. D., & Crisp, D. 1999, Icarus, 138, 36
Knapp, W. H., Stammes, P., & Koelemeijer, R. B. A. 2002, J. Atmos. Sci., 59, 83
Krijger, J. M., Aben, I., & Schrijver, H. 2005, Atmos. Chem. Phys., 5, 2729
Montañés-Rodriguez, P., Pallé, E., & Goode, P. R. 2005, ApJ, 629, 1175
Mustard, J. F., & Bell, J. F., III. 1994, Geophys. Res. Lett., 21, 353
Oliva, E., & Origlia, L. 1992, A&A, 254, 466
Seager, S., Turner, E. L., Schafer, J., & Ford, E. B. 2005, Astrobiology, 5, 372
Tinetti, G., Meadows, V. S., Crisp, D., Fong, W., Fishbein, E., Turnbull, M. C., & Bibring, J. P. 2006a, Astrobiology, 6, 34
Tinetti, G., Meadows, V. S., Crisp, D., Kiang, N., Kahn, B. H., Bosc, E., Fishbein, E., Velusamy, T., & Turnbull, M. C. 2006b, Astrobiology, in press
Traub, W. A. 2003, in ASP Conf. Ser. 294, Scientific Frontiers in Research on Extrasolar Planets, ed. D. Deming & S. Seager (San Francisco: ASP), 595
Traub, W. A., & Jucks, K. 2002, in Atmospheres in the Solar System: Comparative Aeronomy, ed. M. Mendillo, A. Nagy, & J. H. Waite (Geophys. Monogr. 130; Washington: AGU), 369
Traub, W. A., & Stier, M. T. 1976, Appl. Optics, 15, 364
Wilson, J. C., et al. 2001, PASP, 113, 227
Woolf, N. J., Smith, P. S., Traub, W. A., & Jucks, K. W. 2002, ApJ, 574, 430 (Paper I)